Nanoscale Advances

PAPER

View Article Online
View Journal | View Issue

Cite this: *Nanoscale Adv.*, 2025, 7, 5080

Enhanced electrocatalytic performance of $NiCo_2O_4$ nanosheets and nanoribbons for methanol oxidation in alkaline media: morphology-dependent insights

Hagar Ali,[a] Waleed M. A. El Rouby,[a] M. H. Khedr[a] and Mai F. M. Hmamm*[b]

$NiCo_2O_4$ nanosheets and nanoribbons were synthesized by calcining Ni–Co hydroxide and Ni–Co MOF precursors at 350 °C for two hours. These precursors were first synthesized *via* hydrothermal and solvothermal techniques, with the goal of improving their efficiency in methanol electro-oxidation. These two different methodologies are the factors that affect the morphology and electrochemical performance of the resulting $NiCo_2O_4$ under the same environmental conditions. The superior characteristics of $NiCo_2O_4$ nanosheets, which showed high crystallinity, well-defined morphology, high porosity, and substantial surface area, were confirmed by X-ray diffraction (XRD), scanning electron microscopy (SEM), energy dispersive spectroscopy (EDS), transmission electron microscopy (TEM), and nitrogen sorption measurements. Chronoamperometry (CA), electrochemical impedance spectroscopy (EIS), and cyclic voltammetry (CV) were used in an alkaline medium to perform electrochemical assessments for methanol oxidation. Remarkably, $NiCo_2O_4$ nanosheets demonstrated excellent electrocatalytic activity, outperforming $NiCo_2O_4$ nanoribbons with a minimal starting potential (0.32 V), elevated current density (70.36 mA cm^{-2}), and good electro-oxidation stability (86%). Their distinct shape, which provides a high surface area and numerous functional sites for reaction, as well as enabling quick ion movement between the electrolyte and the electrode, is credited for the nanosheets' increased electrocatalytic efficiency. These results emphasize the potential of $NiCo_2O_4$ nanosheets as electroactive catalysts for fuel cell applications.

Received 5th March 2025
Accepted 25th June 2025

DOI: 10.1039/d5na00223k

rsc.li/nanoscale-advances

1. Introduction

The search for renewable, clean energy sources to replace depleting fossil fuels, which contribute to environmental issues like air pollution and harmful emissions, is a pressing challenge. The growing global population, coupled with the growth of electric vehicles and portable devices, further exacerbates the need for energy.[1] When compared to conventional energy technologies, fuel cells have attracted a lot of interest because of their high efficiency in converting chemical energy into electrical energy and minimal emissions of pollutants. This has made fuel cells a viable technology for sustainable power generation.[2,3] The many benefits that methanol as a fuel source offers make direct methanol fuel cells (DMFCs) a viable option for producing heat and electricity. These benefits include its low operating temperature, easy availability, affordability, ease of storage and transport, manageability, and large energy density.[3,4] The catalytic performance of electrocatalysts in DMFCs is mostly determined by the methanol oxidation reaction (MOR). While platinum-based catalysts and their alloys exhibit high catalytic activity for the MOR, their high cost, scarcity, and tendency to be poisoned by adsorbed carbon monoxide (CO) on the anode surface, which blocks active sites and leads to incomplete oxidation and slow MOR kinetics, limit their commercial viability.

Additionally, methanol crossover from the anode to the cathode through the proton exchange membrane causes large overpotentials.[5–8] As a result, significant research efforts are focused on developing non-precious electrocatalysts that can enhance the effectiveness of DMFCs by improving methanol electro-oxidation at the anode, facilitating large-scale commercial applications.[9] Because of their availability, low cost, and promising electrocatalytic activity, transition metal oxides have recently gained attention as possible alternatives to noble metal catalysts. Transition metal oxides, including NiO,[10] Co_3O_4,[11] and $NiCo_2O_4$,[12] have been investigated for their potential applications in DMFCs. However, both NiO and Co_3O_4 suffer from slow electron transfer rates and limited catalytic efficiency, which negatively impact their conductivity.[13] Multi-component catalysts, formed by combining

---

[a] Materials Science and Nanotechnology Department, Faculty of Postgraduate Studies for Advanced Sciences (PSAS), Beni-Suef University, 62511 Beni-Suef, Egypt. E-mail: mai.farg@psas.bsu.edu.eg; mai_farge@yahoo.com

[b] Renewable Energy Science and Engineering Department, Faculty of Postgraduate Studies for Advanced Science, Beni-Suef University, 62511 Beni-Suef, Egypt

transition metals and oxides, offer enhanced properties such as improved stability in alkaline pH and poison resistance, often through synergistic effects instead of the independent action of each component.[12,14] This highlights the ongoing research focus on designing composite catalysts to optimize performance. $NiCo_2O_4$, with its spinel structure formed by incorporating Ni atoms into Co_3O_4, has gained widespread use in supercapacitors,[15–17] lithium-ion batteries,[18] and chlorine evolution[19] and oxygen evolution reactions.[20] Rich redox reactions and improved electrical conductivity— two times larger than those of $Co3O_4$ and NiO—are only two benefits of this spinel structure. Fast electron transport is made possible by this increased conductivity, which makes $NiCo_2O_4$ a viable option for electrochemical applications.[21] The effectiveness of $NiCo_2O_4$, however, varies with different morphologies of the electrode material.[22–24] Previous studies have reported various morphologies of $NiCo_2O_4$, including nanorods for methanol oxidation electrocatalysis,[25] coral-like structures having a current density of 21 mA cm^{-2},[26] mesoporous spinel nanoparticles having a current density of 93 mA cm^{-2},[27] and 3D hierarchical hollow microspheres with a current density of 95 mA cm^{-2}.[24] These findings show how the electrochemical characteristics of the final materials are affected by the synthesis conditions and preparation techniques.

Given these considerations, the present study explores the synthesis of $NiCo_2O_4$ under varying methodologies, leading to different morphologies and corresponding changes in electrochemical properties. Both synthesis procedures are cost-effective, straightforward, and time-efficient, with all necessary materials readily available. The resultant $NiCo_2O_4$ nanosheets and nanoribbons are described and evaluated as methanol oxidation electrocatalysts. Interestingly, the methanol oxidation process is highly electrocatalyzed by the $NiCo_2O_4$ nanosheets.

2. Materials and methods

2.1 Materials

The materials, which include nickel nitrate hexahydrate (Ni $(NO_3)_2 \cdot 6H_2O$), cobalt nitrate hexahydrate (Co $(NO_3)_2 \cdot 6H_2O$), 2-methyl imidazole, urea ($CO(NH_2)_2$), ethanol, potassium hydroxide, Nafion solution (5 wt%), and isopropanol, were all of high purity and used straight away without additional processing. For the duration of the investigation, distilled water was employed in the preparation of all solutions.

2.2 Preparation of $NiCo_2O_4$ nanosheets

$NiCo_2O_4$ nanosheets were created through a hydrothermal method. In this process, the metal precursors $Co(NO_3)_2 \cdot 6H_2O$ (0.727 g, 25 mmol), Ni $(NO_3)_2 \cdot 6H_2O$ (0.3634 g, 12.5 mmol), and urea (1.126 g, 187.5 mmol) were dissolved using 100 mL of distilled water under vigorous magnetic stirring for 10 minutes. The resulting mixture was then conveyed into a 100 mL Teflon-lined stainless-steel autoclave and heated at 120 °C for 12 hours. After the reaction, the materials were collected by centrifugation, washed several times with distilled water and ethanol, and dried at 60 °C for 24 hours. The dehydrated powder was subsequently calcined at 350 °C for 2 hours in air to obtain the $NiCo_2O_4$ nanosheets.

2.3 Synthesis of $NiCo_2O_4$ nanoribbons

Using a solvothermal method, $NiCo_2O_4$ nanoribbons were created first by synthesizing the bimetallic Ni–Co/MOF based on a previously published technique.[28] To do this, 25 mmol of Co $(NO_3)_2 \cdot 6H_2O$ and 12.5 mmol of $Ni(NO_3)_2 \cdot 6H_2O$ were mixed with 80 mL of distilled water when vigorously stirred using a magnetic stirrer for 10 minutes. 375 mmol of 2-methylimidazole (2-MeIm) was then suspended in 20 mL of distilled water and stirred until completely dissolved.

The two solutions were then combined together, and the resulting solution was stirred vigorously at 35 °C for 6 hours before being cooled to room temperature. Following cooling, the lavender-colored solution was separated by centrifugation, rinsed with a water–ethanol mixture three times to eliminate any remaining unreacted reagents, and then dried at 60 °C for 24 hours. The resulting Ni–Co MOF was then employed as a template and calcined at 350 °C for 2 hours in air to produce the $NiCo_2O_4$ nanoribbons.

2.4 Characterization techniques

Using Cu Kα radiation (wavelength = 1.54045 Å), an accelerating voltage of 40 kV, and a current of 35 mA, X-ray diffraction (XRD) with a PANalytical Empyrean diffractometer (Netherlands) was used to study the crystal structure and phase identification of the produced materials. A scanning electron microscope (SEM, Sigma 500 VP, Zeiss Microscopy GmbH, Germany) was used to analyze the surface morphology. The materials' surface structure was thoroughly examined using high-resolution transmission electron microscopy (HRTEM, JEOL JEM 2100, Japan).

By combining SEM with Energy Dispersive X-ray Analysis (EDX), the elemental composition was ascertained. Using a Brunauer–Emmett–Teller (BET) analyzer (Tri-Star II 3020, Micromeritics, USA), the surface area and pore size distribution of the nanomaterials were ascertained using nitrogen adsorption–desorption isotherms.

2.5 Preparation of the working electrodes

Prior to usage, the glassy carbon (GC) electrode, which has an active surface area of 0.0706 cm^2, was meticulously polished to a mirror-like surface using aqueous alumina over smooth emery paper. After that, distilled water was used to give it a thorough cleaning. 400 μL of isopropanol and 10 μL of Nafion solution (5 wt%.) were combined with 5.0 milligram of the produced catalysts to create the electrode. To guarantee even dispersion, the mixture was sonicated for 30 minutes at room temperature. Then, in many applications, 15 μL of the sonicated solution was cast onto the GC electrode's active area. To create the functioning electrode, the electrode was lastly dried for 30 minutes at 60 °C.

2.6 Electrochemical measurements

A three-electrode setup including an Ag/AgCl reference electrode with a 3 M KCl solution, a counter electrode to complete the electrical circuit, and a glassy carbon (GC) electrode as the

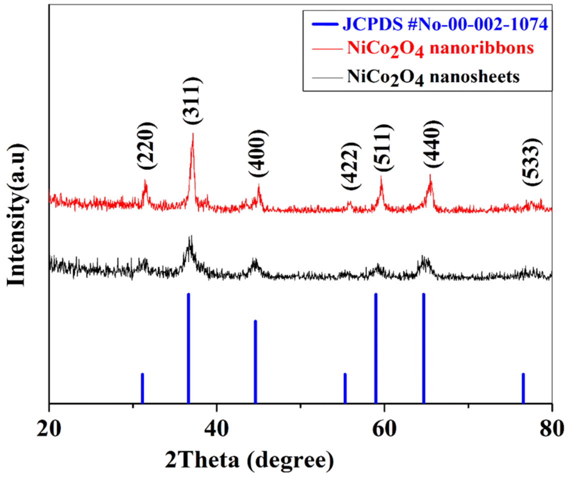

Fig. 1 XRD patterns of the as-prepared $NiCo_2O_4$ nanosheets and nanoribbons.

working electrode—all produced as previously mentioned—was used to perform electrochemical experiments. To assess the electrocatalytic activity of the produced catalysts, all three electrodes were washed with an aqueous electrolyte solution of 1 M KOH, both with and without methanol. At scan speeds ranging from 10 mV s^{-1} to 100 mV s^{-1}, cyclic voltammetry (CV) measurements were carried out within a potential window of 0 to 0.6 V. Chronoamperometry (CA) experiments were performed for 3600 seconds at 0.6 V.

The examination was carried out by Electrochemical Impedance Spectroscopy (EIS) at 0.4 V in the frequency range of 10 kHz to 0.01 Hz. A potentiostat/galvanostat (AUTOLAB PGSTAT 302N, Metrohm, Switzerland) was used for all electrochemical experiments, and it was operated by NOVA 1.11 software.

3. Results and discussion

3.1 Structure and morphological analysis

X-ray diffraction (XRD) analysis was performed to verify the crystallinity and phase structure from the prepared materials, namely $NiCo_2O_4$ nanosheets and $NiCo_2O_4$ nanoribbons. Fig. 1 displays the XRD patterns of $NiCo_2O_4$ for both morphologies. The XRD patterns reveal that all diffraction peaks of the two samples are consistent with the standard spectrum of cubic spinel $NiCo_2O_4$ (JCPDS, no. 00-002-1074). The seven diffraction peaks observed at $2\theta = 31.4°$, 36.65°, 44.6°, 55.5°, 59°, 64.7°,

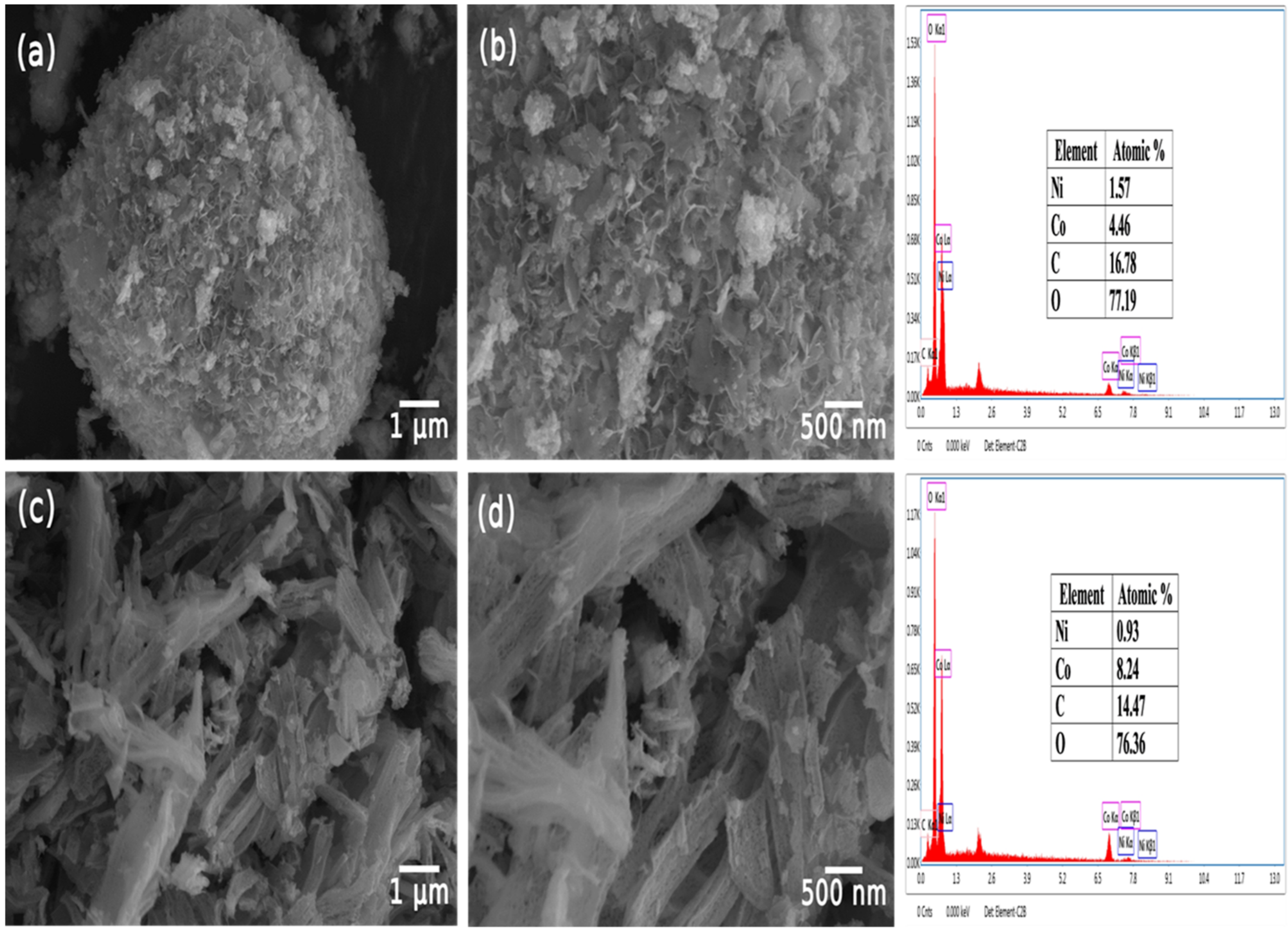

Element	Atomic %
Ni	1.57
Co	4.46
C	16.78
O	77.19

Element	Atomic %
Ni	0.93
Co	8.24
C	14.47
O	76.36

Fig. 2 FESEM images of the as-prepared $NiCo_2O_4$ nanosheets (a and b) and $NiCo_2O_4$ nanoribbons (c and d) with the respective EDS spectrum.

and 77° are characteristic of the (220), (311), (400), (422), (511), (440), and (533) planes of spinel $NiCo_2O_4$, respectively. It is observed that the $NiCo_2O_4$ nanoribbons exhibit slightly higher intensity compared to the $NiCo_2O_4$ nanosheets, suggesting that the crystallinity of the nanoribbons is higher than that of the nanosheets. The intensity of the (311) plane is notably higher in both samples, as well as in the standard reference card, compared to other planes. No other peaks were noted, confirming the high purity and exceptional quality of these catalysts.

The crystallite size (d) of the $NiCo_2O_4$ nanosheets and nanoribbons was estimated using the Debye–Scherrer equation,[29] which is given by:

$$d_{\text{XRD}} = \frac{0.9\lambda}{\beta \cos \theta} \tag{1}$$

where d_{XRD} represents the crystal plane size, λ is the wavelength of the incident X-ray radiation (Cu Kα, 0.15406 nm), β is the full width at half maximum (FWHM), and θ is the angle at the peak maximum. Using eqn (1), the crystallite sizes were calculated to be approximately 11 nm for $NiCo_2O_4$ nanosheets and 44 nm for $NiCo_2O_4$ nanoribbons, based on the high-intensity diffraction peak (311). It is observed that the $NiCo_2O_4$ nanosheets have a smaller crystallite size, which suggests they possess a higher catalytic activity and a larger number of active sites.

The surface morphology of the synthesized samples using different methodologies was analyzed through scanning electron microscopy (SEM) at various magnifications, as presented in Fig. 2 (a–d). Fig. 2(a) and (b) reveal that $NiCo_2O_4$, synthesized from calcined Ni–Co hydroxide (hydrothermal route), consists of several interconnected thin nanosheets that are randomly distributed and connected to form porous microspheres at the microscale. Fig. 2(c) and (d) show the morphology of $NiCo_2O_4$ produced from calcined Ni–Co MOF (solvothermal route), where the material is composed of a collection of strips that aggregate to form nanoribbons with high porosity. These nanoribbons offer numerous active sites for chemical reactions, making the material suitable for further modification and improving its properties for various applications.

The huge impact of the synthesis method on the surface morphology and particle size of the final sample is observed, where the surface morphology is changed according to the synthesis method used. The hydrothermal approach produces $NiCo_2O_4$ nanosheets by subjecting it to a constant pressure heat treatment for 12 hours at 120 °C. Similar to this, continuous stirring in the solvothermal method causes the uniformity in the morphology that results in nanoribbons in addition to large surface area.

Energy Dispersive X-ray Spectroscopy (EDS) was employed to analyze the elemental composition and chemical properties of the catalysts. The EDS findings verified the purity of both $NiCo_2O$ nanosheets and nanoribbons, revealing that they consisted exclusively of Ni, Co, C, and O, as shown in Fig. 2.

While the carbon content, likely residual from the 2-methylimidazole precursor, is notable, it is not expected to significantly impact the catalytic performance, as the predominant

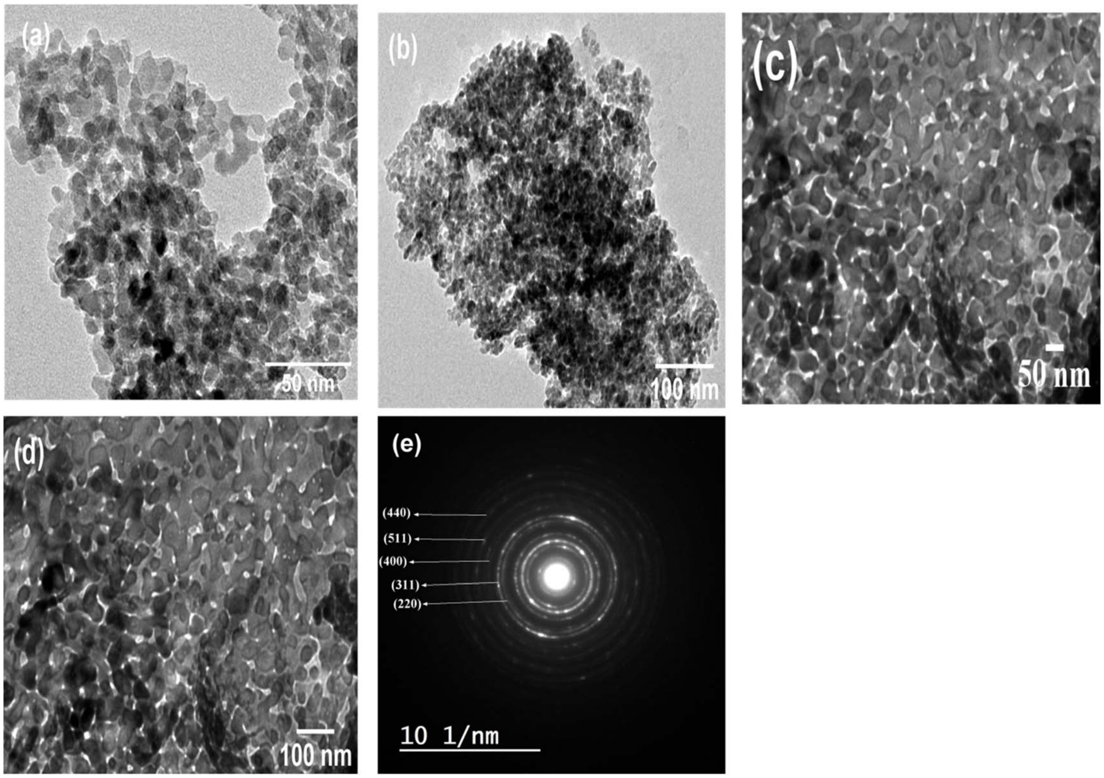

Fig. 3 TEM images of the as-prepared $NiCo_2O_4$ nanosheets (a and b) and $NiCo_2O_4$ nanoribbons (c and d), and SAED pattern of $NiCo_2O_4$ nanosheets (e).

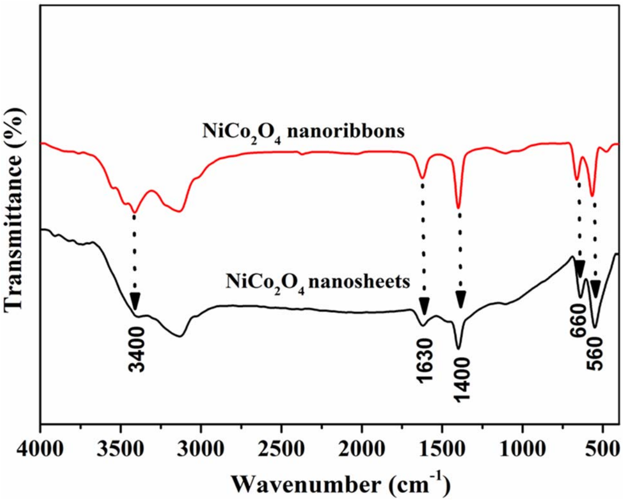

Fig. 4 FTIR of $NiCo_2O_4$ nanosheets and $NiCo_2O_4$ nanoribbons.

phases are $NiCo_2O$. However, the carbon could potentially influence the material's conductivity, contributing slightly to electron transport. These findings further support the purity of the nanoribbons and nanosheets and offer insights into the role of residual carbon in the overall properties of the catalysts.

Fig. 3(a–e) display the Transmission Electron Microscopy (TEM) images and Selected Area Electron Diffraction (SAED) patterns, which were utilized to further analyze the internal microstructure and crystallographic characteristics of $NiCo_2O_4$ nanosheets and nanoribbons, supporting the morphology observed in the SEM images. The TEM images of $NiCo_2O_4$ nanosheets in Fig. 3(a) and (b) show a spherical shape, with nanosheets positioned at the ends of the microspheres, exhibiting a compact structure. At higher magnification (Fig. 3(b)), voids within the particles are observed, suggesting a porous surface structure of the nanosheets.

The TEM images of $NiCo_2O_4$ nanoribbons in Fig. 3(c) and (d) confirm the helical structure of the ribbons observed in the SEM images. Additionally, Fig. 3(d) highlights the porous nature of the ribbons, with empty regions between the particles, further emphasizing their high porosity. This porous structure in both the $NiCo_2O_4$ nanosheets and nanoribbons plays a crucial role in providing numerous electroactive sites, facilitating electron transfer from the electrolyte to the anode, and enhancing the reaction rate.

The SAED pattern of $NiCo_2O_4$ in Fig. 3(e) further confirms the polycrystalline nature of the synthesized material, showing clearly defined rings. Consistent with the X-ray diffraction (XRD) results, all the rings in the SAED pattern can be related to the characteristic planes of $NiCo_2O_4$.

3.2 FTIR analysis

Fourier-transform infrared (FTIR) spectroscopy was conducted over a wide wavenumber range (400–4000 cm^{-1}) to investigate the functional groups in $NiCo_2O_4$ (Fig. 4). The band at 3400 cm^{-1} and the peak at 1630 cm^{-1} are attributed to specific vibrational modes. The 3400 cm^{-1} band is associated with the bending vibration of hydrogen-bonded hydroxyl groups (H–O–H), while the peak at 1630 cm^{-1} corresponds to the stretching vibrations of hydroxyl groups attached to metal oxides. A broad peak around 1400 cm^{-1} demonstrates the presence of NO_3^- anions. Furthermore, two distinct bands near 660 cm^{-1} and 560 cm^{-1} are observed, which are related to metal–oxygen

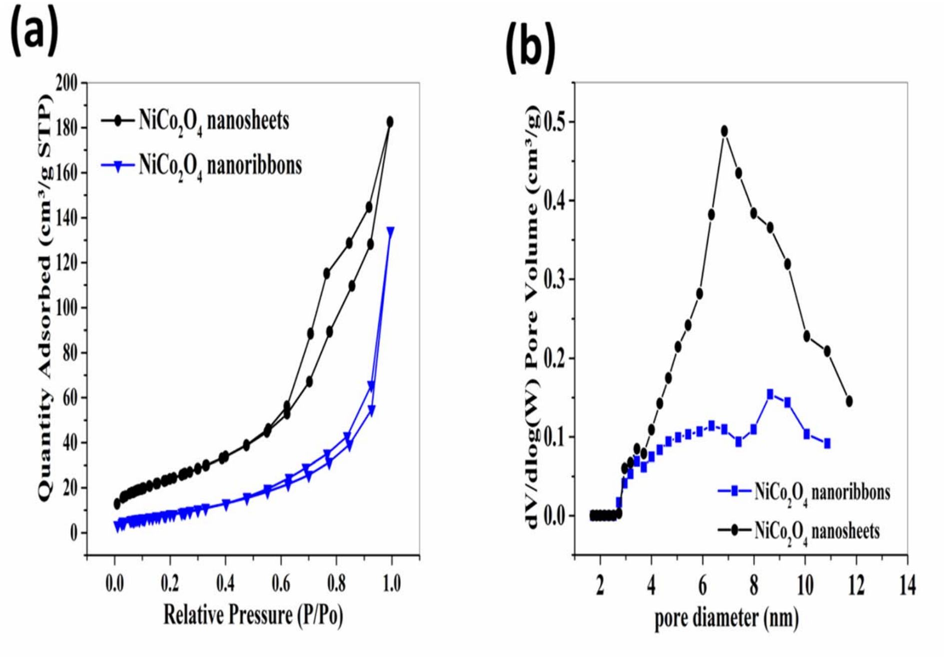

Fig. 5 (a) Nitrogen adsorption/desorption isotherms for $NiCo_2O_4$ nanosheets and nanoribbons, (b) pore size distribution of $NiCo_2O_4$ nanosheets and nanoribbons.

Table 1 Surface area analysis of $NiCo_2O_4$ nanosheets and nanoribbons

Samples	S_{BET} ($m^2\ g^{-1}$)	Pore volume ($cm^3\ g^{-1}$)	Pore size (nm)
$NiCo_2O_4$ nanosheets	89	0.279	6.8
$NiCo_2O_4$ nanoribbons	32	0.2	8.6

bonds in a cubic spinel structure, where Ni^{2+} or Co^{2+} ions are tetrahedrally coordinated with oxygen.[30] These metal–oxygen bands may shift if the bond lengths of cations and anions at the tetrahedral and octahedral sites change.[31]

3.3 Brunauer Emmett Teller (BET) surface area analysis

Nitrogen adsorption–desorption isotherms, along with the Barrett–Joyner–Halenda (BJH) method, were used to determine the surface area and pore size distribution of the synthesized samples, as presented in Fig. 5(a) and (b). The structural properties of the samples, described in Table 1, show that the $NiCo_2O_4$ nanosheets have a surface area of 89 $m^2\ g^{-1}$, which is approximately three times higher than that of the $NiCo_2O_4$ nanoribbons. Both the $NiCo_2O_4$ nanosheets and nanoribbons exhibit a type IV isotherm with H3-type hysteresis loops at $P/P_0 >$ 0.4, indicating their mesoporous characteristics. TEM images (Fig. 5a and d) further support these findings, showing visible

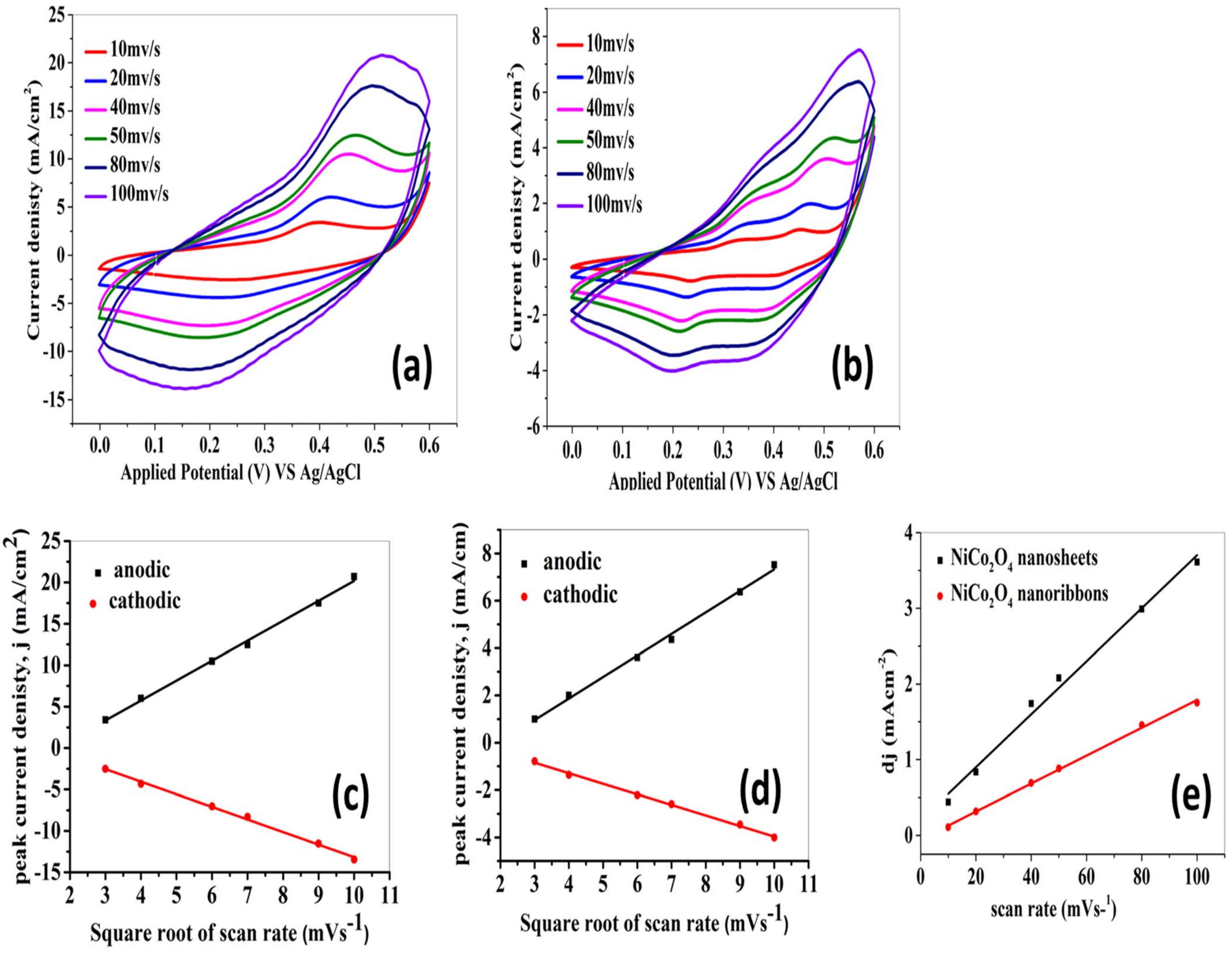

(f)

	$NiCo_2O_4$ nanosheets	$NiCo_2O_4$ nanoribbons
ECSA (cm^2)	1.89	0.8

Fig. 6 Cyclic voltammetry of (a) $NiCo_2O_4$ nanosheet and (b) $NiCo_2O_4$ nanoribbon electrodes in 1.0 M KOH at various scan rates. Panels (c) and (d) show the correlation between anodic and cathodic current densities and the square root of the scan rate for $NiCo_2O_4$ nanosheets and nanoribbons, respectively. (e) Average current density ($dj = (j_a - j_c)/2$) against the scan rate showing the double-layer capacitance (C_{dl}) extracted from the corresponding CVs. (f) table displaying the electrochemical active surface area (ECSA).

interconnections between nanoparticles and confirming the mesoporous structure.

The material's high surface area improves the kinetics of electrochemical reactions by promoting greater electron transfer, thereby offering more active sites for catalysis. Additionally, a larger pore volume allows for a greater quantity of ions to be stored within the electrode material, promoting easier ion mobility and improving overall electrochemical performance.[32–34]

3.4 Electrochemical activity

The electrochemical activity of the prepared $NiCo_2O_4$ nanosheet and $NiCo_2O_4$ nanoribbon modified glassy carbon (GC) electrodes was assessed using cyclic voltammetry in 1 M KOH at scan rates of 10, 20, 40, 50, 80, and 100 mV s^{-1} within a potential range of 0 to 0.6 V (*vs.* Ag/AgCl). The cyclic voltammograms, shown in Fig. 6, exhibit anodic and cathodic peaks corresponding to the oxidation states of Ni^{2+}/Ni^{3+} and Co^{2+}/Co^{3+} for both modified GC electrodes, signifying the charge transfer processes of these metal ions.[32,33] No additional peaks were observed when the bare glassy carbon electrode was tested within the same potential range, as seen in Fig. 7(a). The dual redox reactions of Ni^{2+}/Ni^{3+} and Co^{2+}/Co^{3+} serve as electroactive centers, promoting the electro-oxidation of methanol.[37] These redox processes in an alkaline medium can be described by the equation provided in previous studies.[33,35,36]

$$NiCo_2O_4 + OH^- + H_2O \rightarrow NiOOH + 2CoOOH + e^- \quad (2)$$

Fig. 6(a) and (b) display the cyclic voltammetry data for $NiCo_2O_4$ nanosheets and nanoribbons in 1 M KOH at scan rates ranging from 10 to 100 mV s^{-1}, demonstrating an increase in current density with higher scan rates. The anodic and cathodic redox peaks show a linear dependence on the square root of the scan rate (10 to 100 mV s^{-1}), suggesting that the electrochemical processes are surface-controlled,[40] as depicted in Fig. 6(c) and (d). Fig. 6(e) shows the double layer capacitance (C_{dl}) extracted from a CV according to the equation: $C_{dl} = dj(j_a - j_c)/2\nu$, where j_a and j_c are anodic and cathodic current densities and ν is the scan rate in mV s^{-1}. Electrochemical surface area as non-faradaic current density was determined from the equation: ECSA = C_{dl}/C_s, where C_s is the electrode's specific capacitance, which was calculated to be 0.022 mF cm^{-2} in an electrolyte of 1 M KOH. Therefore, the estimated ECSA is shown as a table in Fig. 6(g).

As depicted in Fig. 7(a), the $NiCo_2O_4$ nanosheets show wider redox peaks and a larger integrated CV area compared to the $NiCo_2O_4$ nanoribbons, suggesting superior catalytic activity for the nanosheets. These results align with the surface area data in Table 1. Previous research has indicated that a higher surface area is associated with better catalytic performance.[34,38,39] Thus, the enhanced electrocatalytic performance of the $NiCo_2O_4$ nanosheets can be attributed to their greater surface area and pore volume.[41,42]

Cyclic voltammetry was used to assess the electrocatalytic activity of the synthesized $NiCo_2O_4$ nanosheets and nanoribbons in a 1 M KOH electrolyte with varying methanol concentrations, over a potential range of 0 to 0.6 V, to evaluate methanol electrooxidation. Upon adding methanol to the KOH electrolyte, the

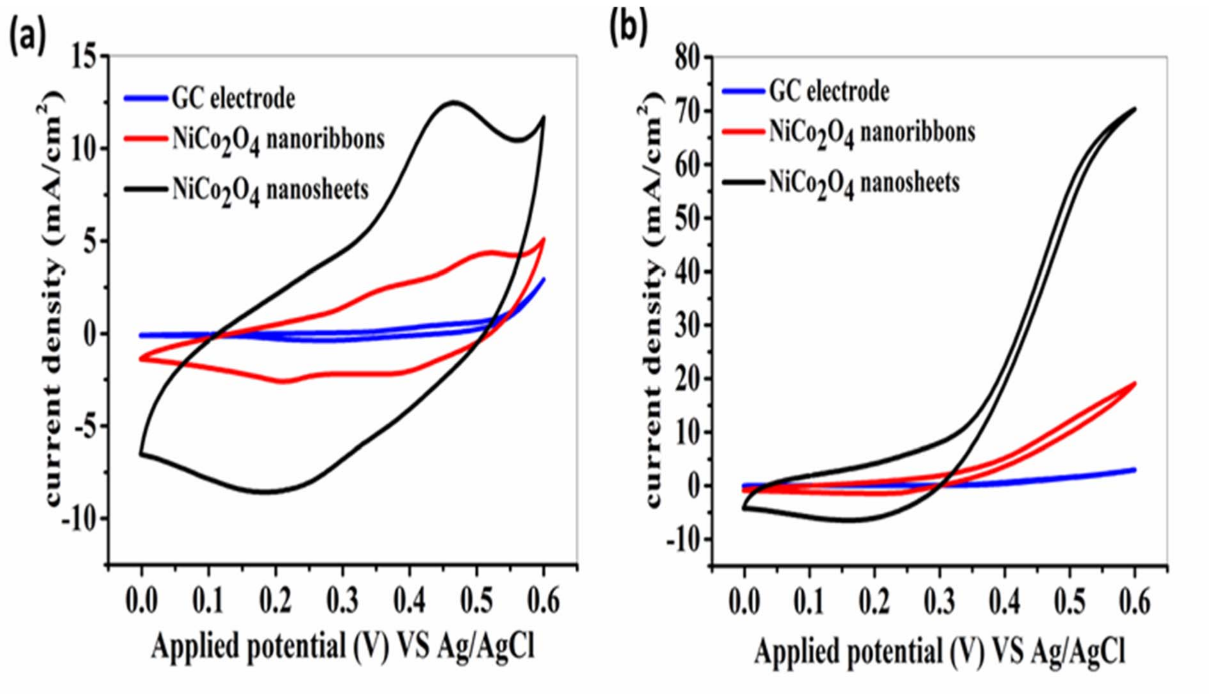

Fig. 7 Comparison of CV curves of $NiCo_2O_4$ Nanosheets, $NiCo_2O_4$ Nanoribbons and the GC electrode at a scan rate of 50 mV s^{-1} in (a) 1 M KOH and (b) 3 M methanol.

Table 2 A comparison of the electrochemical activity of the $NiCo_2O_4$ nanosheet and $NiCo_2O_4$ nanoribbon electrocatalysts for the methanol oxidation reaction with that of previously reported catalysts

Electrocatalyst	Morphology	Current density (mA cm^{-2})	Ref.
$NiCo_2O_4$	Nanosheets	70.36	This work
$NiCo_2O_4$	Nanoribbons	19	This work
$NiCo_2O_4$/rGO	Hexagonal	16.6	37
$NiCo_2O_4$	Nanoplates	12.0	37
$NiCo_2O_4$	Urchin-like	8.85	36
$NiCo_2O_4$	Sheaf-like	7.31	36
$NiCo_2O_4$	Coral-like	21	26
$NiCo_2O_4$/rGO	Nanorods	78	35
β-Ni(OH)-$NiCo_2O_4$	Nanorods	20	44

redox peaks associated with Ni^{2+}/Ni^{3+} and Co^{2+}/Co^{3+} disappeared, and a distinct methanol oxidation peak appeared at 0.32 V for $NiCo_2O_4$ nanosheets and 0.43 V for $NiCo_2O_4$ nanoribbons (*vs.* Ag/AgCl). Notably, the onset potential (indicating the start of the redox reaction) was lower for the $NiCo_2O_4$ nanosheets, requiring less energy for the redox processes compared to the $NiCo_2O_4$ nanoribbons.[43] In addition to the onset potential, the catalytic current density plays a key role in determining the electrocatalytic proficiency of the electro-oxidation reaction. $NiCo_2O_4$ nanosheets demonstrated a higher current density of approximately 70.36 mA cm^{-2}, while $NiCo_2O_4$ nanoribbons produced only about 19 mA cm^{-2} in 3 M KOH and at 50 mV s^{-1}, indicating superior electrocatalytic activity for methanol electro-oxidation in the nanosheets. Furthermore, the performance of $NiCo_2O_4$ nanosheets surpasses that of previously reported $NiCo_2O_4$ and its modified versions in methanol electro-oxidation, as summarized in Table 2.

An increase in current density was observed as the KOH concentration (MeOH) was raised from 0.5 to 3 M, followed by a slight decrease as the MeOH concentration continued to increase beyond 3 M, as shown in Fig. 8(a) for $NiCo_2O_4$ nanosheets. In contrast, for $NiCo_2O_4$ nanoribbons, the current density increased with KOH concentration from 0.5 to 4 M, after which it started to decrease at concentrations higher than 4 M, as shown in Fig. 8(b). Fig. 8(c) and (d) display the electrochemical activity of $NiCo_2O_4$ nanosheets under different methanol concentrations of 0.5, 1, 3, 4, and 5 M.

3.5 Methanol electro-oxidation mechanism

The electro-catalytic mechanism for the methanol oxidation reaction on the $NiCo_2O_4$ electrode is briefly explained according to the following reactions:[45,46]

$$CoOOH + OH^- \rightarrow CoO_2 + H_2O + e^- \quad (3)$$

$$Ni(OH)_2 + OH^- \rightarrow NiOOH + H_2O + e^- \quad (4)$$

As shown in Fig. 8, the addition of 0.5 M methanol to 1 M KOH leads to an increase in current density at 0.6 V, which is

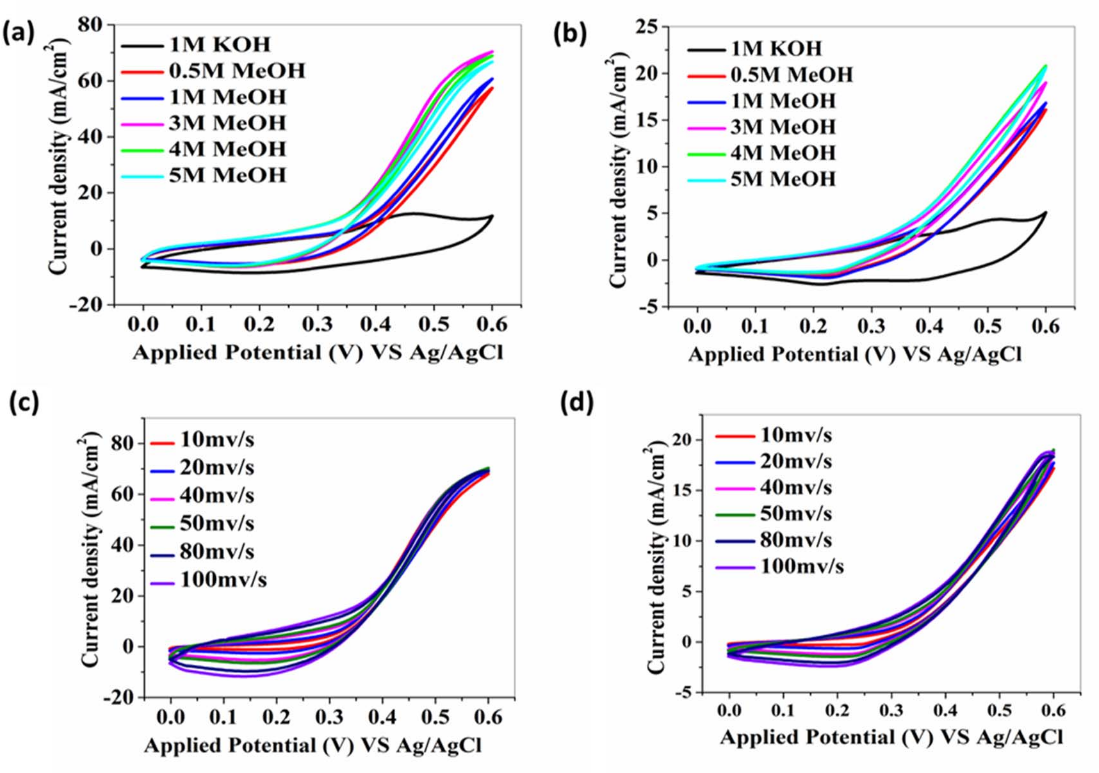

Fig. 8 Cyclic voltammetry of (a) $NiCo_2O_4$ nanosheet and (b) $NiCo_2O_4$ nanoribbon electrodes at various methanol concentrations and a scan rate of 50 mV s^{-1}. Panels (c) and (d) show the CV curves of $NiCo_2O_4$ nanosheets and $NiCo_2O_4$ nanoribbons, respectively, at different scan rates and 3 M methanol.

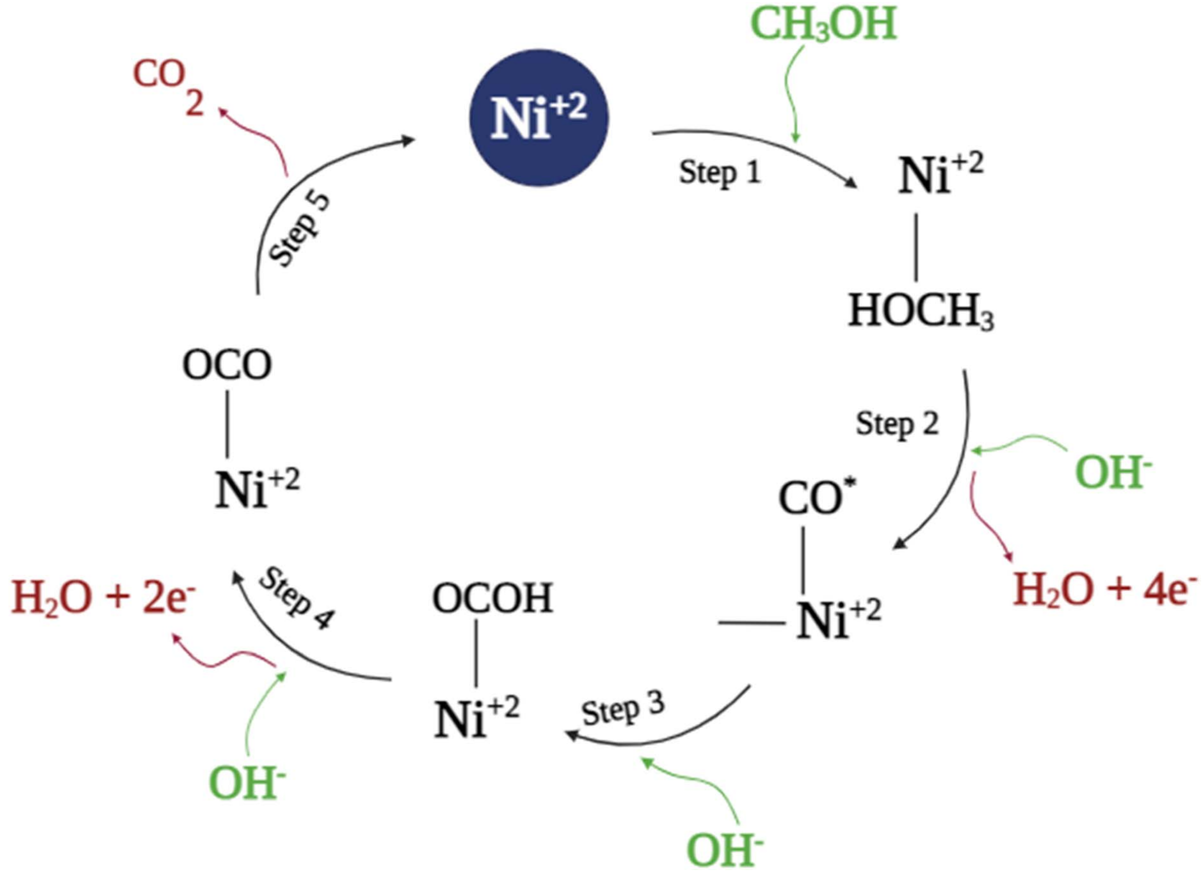

Fig. 9 The suggested mechanism for the methanol oxidation process on the $NiCo_2O_4$ catalyst surfaces.

attributed to the methanol oxidation reaction (MOR) taking place on the surface of the $NiCo_2O_4$ electrode. The MOR on the $NiCo_2O_4$ electrode can be expressed by the following equation:[45,47,48]

$$2MOOH + 2CH_3OH + 5/2O_2 \rightarrow 2M(OH)_2 + 2CO_2 + 3H_2O\ (M = Ni, Co) \quad (5)$$

Fig. 9 illustrates a possible mechanism for the methanol oxidation reaction (MOR) on the $NiCo_2O_4$ electrode. However, the precise mechanism of methanol electro-oxidation in nickel-based catalysts is still a subject of debate. Since Co_3O_4 is thought to be inactive for methanol oxidation as reported by many authors, the Co atom is not shown in Fig. 9.[49] Based on the following net equation of methanol oxidation:[50]

$$CH_3OH + H_2O \rightarrow CO_2 + 6H^+ + 6e^- \quad (6)$$

The complete oxidation of methanol requires the transfer of six electrons, leading to a high overpotential and slow kinetics on the catalyst. As the potential increases, CH_3OH adsorbs (Step 1) on the surface of $NiCo_2O_4$ catalysts, followed by several dehydrogenation steps (Step 2), generating intermediates such as CO_{ads}, CH_2O^-, and CH_3O^-.[51] Since CO_{ads} is considered the primary carbon-containing adsorbate on the catalyst surface during methanol oxidation, CO* is used as a representative species in Fig. 9.[52] At higher potentials, the CO* intermediate

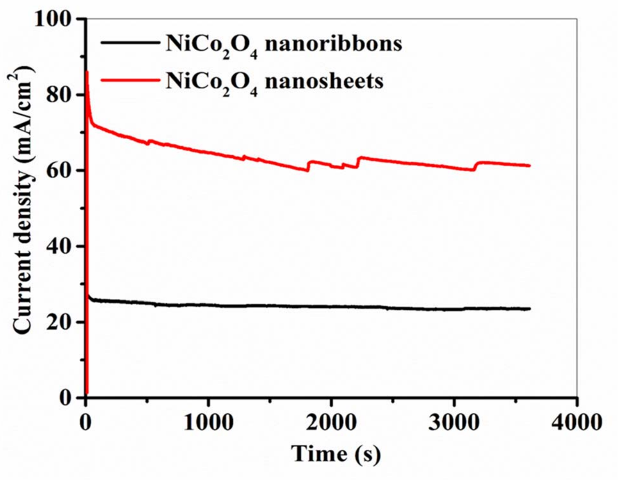

Fig. 10 Chronoamperometry curves for $NiCo_2O_4$ Nanosheets and $NiCo_2O_4$ Nanoribbons electrodes in 1.0 M KOH + 3 M methanol solution at 0.6 V (*vs.* Ag/AgCl).

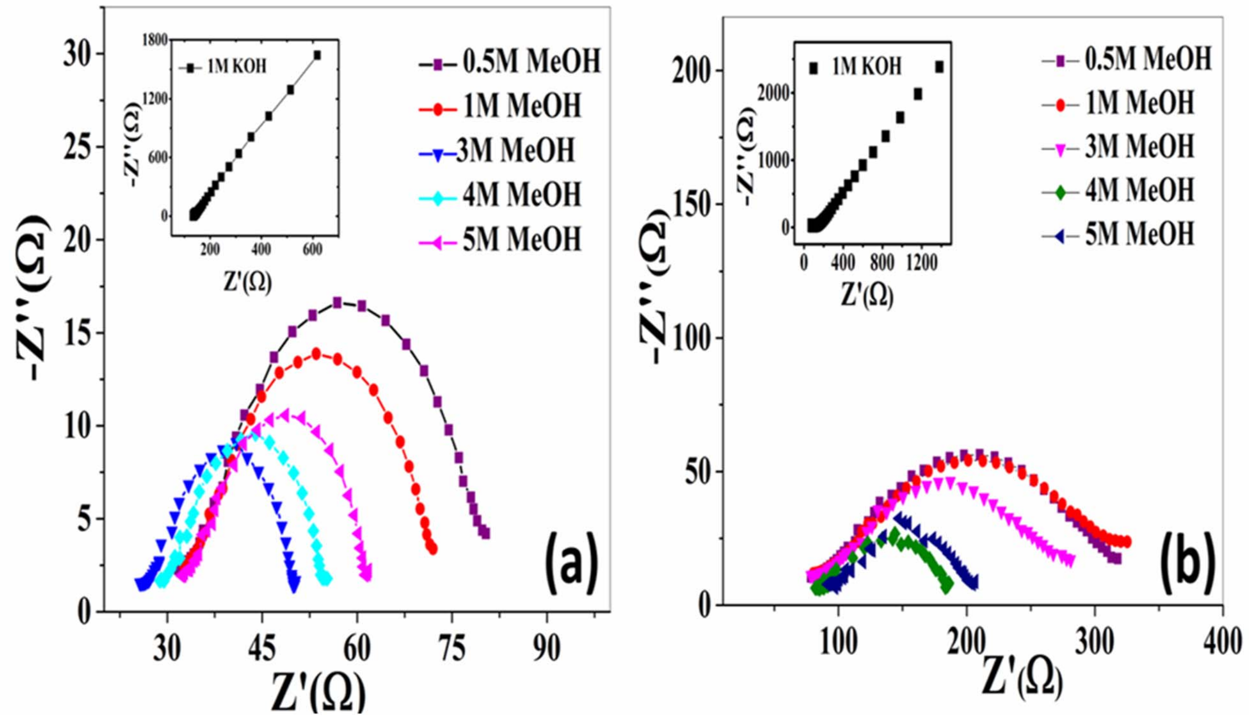

Fig. 11 The Nyquist plots of the studied (a) $NiCo_2O_4$ nanosheets and (b) $NiCo_2O_4$ nanoribbons at different methanol concentrations from 0 M (1 M KOH) to 5 M.

can facilitate the formation of COOH (Step 3). Subsequently, the unstable COOH converts into carbon dioxide (Step 4). Finally, the catalytic sites are regenerated when the produced CO_2 desorbs from the surface (Step 5).

3.6 Stability performance

The electrochemical stability, a crucial factor for evaluating catalytic performance and a significant challenge for commercial applications, was assessed using chronoamperometry. Fig. 10 presents the chronoamperometry results for $NiCo_2O_4$ nanosheets and nanoribbons, tested for stability in 3 M methanol at a constant potential of 0.6 V (*vs.* Ag/AgCl) for 3600 s. The data clearly show that $NiCo_2O_4$ nanosheets achieve a higher maximum current density compared to $NiCo_2O_4$ nanoribbons, indicating a greater number of active sites and superior electrocatalytic performance. These results

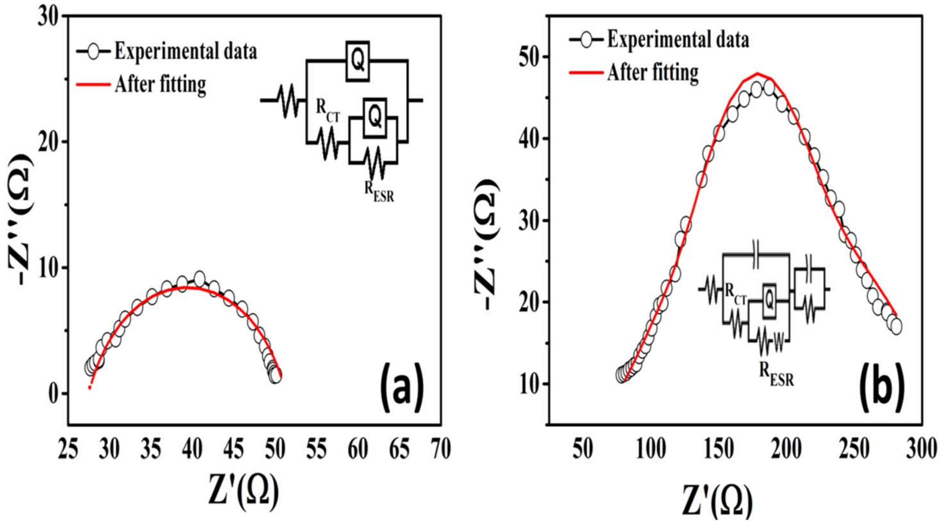

Fig. 12 The difference between the fitted and experimental data of the prepared (a) $NiCo_2O_4$ nanosheets and (b) $NiCo_2O_4$ nanoribbon in 3 M MeOH.

align with those from cyclic voltammetry. Throughout the 3600 s test, both electrodes showed a decrease in current density, likely due to active site blockage by intermediate species, resulting in catalyst poisoning.[53] However, the current retention after 3600 s was significantly higher for the $NiCo_2O_4$ nanosheets, which retained 86% of the initial current, compared to 85% for the $NiCo_2O_4$ nanoribbons, suggesting better catalytic durability for the nanosheets.

3.7 EIS measurements

Electrochemical impedance spectroscopy (EIS) is an essential method for assessing electrode conductivity by measuring its resistance and the equivalent series resistance (ESR) of the cell. EIS was conducted at a potential of 0.4 V over a frequency range from 0.01 to 100 000 Hz, with varying concentrations of methanol (Fig. 11), which demonstrate the highest conductivity at 3 M MeOH compared to the other methanol concentrations. The EIS data is typically presented as a Nyquist plot, where the x-axis intercept at high frequency represents the resistance R_s, which corresponds to the sum of the electrolyte, electronic, and ionic resistances.[54] A semicircle observed at higher frequencies in the plot provides insight into the charge transfer resistance (R_{ct}). The intercept at low frequency thus reflects the total resistance ($R_s + R_{ct}$). The EIS measurements and data fitting were carried out using Nova 1.11 software. Fig. 12 shows the Nyquist plots of $NiCo_2O_4$ nanosheets and $NiCo_2O_4$ nanoribbons, with corresponding semicircle fitting for 3 M MeOH. It is apparent that the semicircle for $NiCo_2O_4$ nanosheets is smaller than that of $NiCo_2O_4$ nanoribbons at the same methanol concentration, indicating lower charge transfer resistance (R_{ct}) and ESR for the nanosheets. Specifically, the R_{ct} and ESR values for $NiCo_2O_4$ nanosheets are 0.048 kΩ and 0.0256 kΩ, respectively, whereas for $NiCo_2O_4$ nanoribbons, they are 0.2 kΩ and 0.07834 kΩ. These findings suggest that $NiCo_2O_4$ nanosheets exhibit faster electron transport and better conductivity.[55]

3.8 Conclusion

In conclusion, $NiCo_2O_4$ nanosheets and nanoribbons were successfully prepared using hydrothermal and solvothermal methods, followed by calcination at 350 °C for 2 hours. Their electrocatalytic performance for methanol oxidation in alkaline media was assessed. The controlled morphology of the materials resulted in $NiCo_2O_4$ nanosheets demonstrating superior electrochemical performance compared to the nanoribbons, as indicated by higher current density, lower onset potential, and improved stability. The increased electrocatalytic activity of the $NiCo_2O_4$ nanosheets can be attributed to several key factors: the synergistic effects of their composition, mesoporous structure, and unique micro-spherical morphology consisting of multiple nanosheets. These characteristics provide a high surface area and promote efficient ionic transport during methanol oxidation. The $NiCo_2O_4$ nanosheet electrode achieved a current density of 70.36 mA cm^{-2} at 0.6 V in 1 M KOH and 3 M CH_3OH electrolytes, with excellent stability, showing 86% current retention over 3600 s. In contrast, the $NiCo_2O_4$ nanoribbons displayed a lower current density of 19 mA cm^{-2} under the same conditions, with 85% current retention over the same duration. These findings offer valuable insights for designing electrocatalysts with optimized morphology to enhance performance in methanol oxidation reactions.

Data availability

The datasets generated during the current study are available from the corresponding author on reasonable request.

Conflicts of interest

There are no conflicts to declare.

Acknowledgements

This study was supported by the Science, Technology & Innovation Funding Authority (STDF) through the grant YRG Call 10, project ID 43211.

References

1 M. S. Rahmanifar, H. Hesari, A. Noori, M. Y. Masoomi, A. Morsali and M. F. Mousavi, A dual Ni/Co-MOF-reduced graphene oxide nanocomposite as a high performance supercapacitor electrode material, *Electrochim. Acta*, 2018, **275**, 76–86, DOI: **10.1016/j.electacta.2018.04.130**.

2 A. Zaher, W. M. A. El Rouby and N. A. M. Barakat, Tungsten incorporation in nickel doped carbon nanofibers as efficient electrocatalyst for ethanol oxidation, *Fuel*, 2020, **280**, DOI: **10.1016/j.fuel.2020.118654**.

3 L. Yaqoob, T. Noor and N. Iqbal, Recent progress in development of efficient electrocatalyst for methanol oxidation reaction in direct methanol fuel cell, *Int. J. Energy Res.*, 2021, **45**(5), 6550–6583, DOI: **10.1002/er.6316**.

4 G. S. Ferdowsi, S. A. Seyedsadjadi and A. Ghaffarinejad, Ni nanoparticle modified graphite electrode for methanol electrocatalytic oxidation in alkaline media, *J. Nanostruct. Chem.*, 2015, **5**(1), 17–23, DOI: **10.1007/s40097-014-0124-z**.

5 T. Noor, *et al.*, Nanocomposites of NiO/CuO based MOF with rGO: An efficient and robust electrocatalyst for methanol oxidation reaction in DMFC, *Nanomaterials*, 2020, **10**(8), 1–18, DOI: **10.3390/nano10081601**.

6 M. B. Askari, P. Salarizadeh, M. Seifi and S. M. Rozati, Ni/NiO coated on multi-walled carbon nanotubes as a promising electrode for methanol electro-oxidation reaction in direct methanol fuel cell, *Solid State Sci.*, 2019, **97**, DOI: **10.1016/j.solidstatesciences.2019.106012**.

7 A. Kaur, G. Kaur, P. P. Singh and S. Kaushal, Supported bimetallic nanoparticles as anode catalysts for direct methanol fuel cells: A review, *Int. J. Hydrogen Energy*, 2021, **46**(29), 15820–15849, DOI: **10.1016/j.ijhydene.2021.02.037**.

8 H. Khuntia, K. S. Bhavani, T. Anusha, T. Trinadh, M. C. Stuparu and P. K. Brahman, Synthesis and characterization of corannulene-metal-organic framework support material for palladium catalyst: an excellent anode

material for accelerated methanol oxidation, *Colloids Surf., A*, 2021, **615**, 126237, DOI: 10.1016/j.colsurfa.2021.126237.

9 S. Gamil, M. Antuch, I. T. Zedan and W. M. A. El Rouby, 3D NiCr-layered double hydroxide/reduced graphene oxide sand rose-like structure as bifunctional electrocatalyst for methanol oxidation, *Colloids Surf., A*, 2020, **602**, 125067, DOI: 10.1016/j.colsurfa.2020.125067.

10 K. Zhang, *et al.*, Interface engineering of Ni/NiO heterostructures with abundant catalytic active sites for enhanced methanol oxidation electrocatalysis, *J. Colloid Interface Sci.*, 2023, **630**, 570–579, DOI: 10.1016/j.jcis.2022.10.057.

11 G. Rajeshkhanna and G. Ranga Rao, Micro and nano-architectures of Co3O4 on Ni foam for electro-oxidation of methanol, *Int. J. Hydrogen Energy*, 2018, **43**(9), 4706–4715, DOI: 10.1016/j.ijhydene.2017.10.110.

12 M. U. Anu Prathap and R. Srivastava, Synthesis of $NiCo_2O_4$ and its application in the electrocatalytic oxidation of methanol, *Nano Energy*, 2013, **2**(5), 1046–1053, DOI: 10.1016/j.nanoen.2013.04.003.

13 A. K. Das, *et al.*, Facile synthesis of $NiCo_2O_4$ nanorods for electrocatalytic oxidation of methanol, *J. Saudi Chem. Soc.*, 2020, **24**(5), 434–444, DOI: 10.1016/j.jscs.2020.03.007.

14 A. K. Das, R. K. Layek, N. H. Kim, D. Jung and J. H. Lee, Reduced graphene oxide (RGO)-supported $NiCo_2O_4$ nanoparticles: An electrocatalyst for methanol oxidation, *Nanoscale*, 2014, **6**(18), 10657–10665, DOI: 10.1039/c4nr02370f.

15 X. Chen, *et al.*, Synthesis and characterization of a $NiCo_2O_4$@$NiCo_2O_4$ hierarchical mesoporous nanoflake electrode for supercapacitor applications, *Nanomaterials*, 2020, **10**(7), 1–13, DOI: 10.3390/nano10071292.

16 X. Wang, Y. Fang, B. Shi, F. Huang, F. Rong and R. Que, Three-dimensional $NiCo_2O_4$@$NiCo_2O_4$ core–shell nanocones arrays for high-performance supercapacitors, *Chem. Eng. J.*, 2018, **344**, 311–319, DOI: 10.1016/j.cej.2018.03.061.

17 M. Sethi and D. K. Bhat, Facile solvothermal synthesis and high supercapacitor performance of $NiCo_2O_4$ nanorods, *J. Alloys Compd.*, 2019, **781**, 1013–1020, DOI: 10.1016/j.jallcom.2018.12.143.

18 W. Wang, X. Song, C. Gu, D. Liu, J. Liu and J. Huang, A high-capacity $NiCo_2O_4$@reduced graphene oxide nanocomposite Li-ion battery anode, *J. Alloys Compd.*, 2018, **741**, 223–230, DOI: 10.1016/j.jallcom.2018.01.097.

19 K. R. Reddy, *An Analytical Study on Supercapacitive Behaviour of $NiCo_2O_4$ Nanoparticles*, vol. X, Ii, 2017, pp. 252–255.

20 F. Paquin, J. Rivnay, A. Salleo, N. Stingelin and C. Silva, Multi-phase semicrystalline microstructures drive exciton dissociation in neat plastic semiconductors, *J. Mater. Chem. C*, 2015, **3**, 10715–10722, DOI: 10.1039/b000000x.

21 Z. Li, *et al.*, Controllable synthesis of graphene/$NiCo_2O_4$ three-dimensional mesoporous electrocatalysts for efficient methanol oxidation reaction, *Electrochim. Acta*, 2017, **252**, 180–191, DOI: 10.1016/j.electacta.2017.09.003.

22 J. Fan, K. Qi, H. Chen, W. Zheng and X. Cui, Morphology dependence of electrochemical properties on palladium nanocrystals, *J. Colloid Interface Sci.*, 2017, **490**, 190–196, DOI: 10.1016/j.jcis.2016.11.061.

23 F. Deng, *et al.*, Controllable Growth of Hierarchical $NiCo_2O_4$ Nanowires and Nanosheets on Carbon Fiber Paper and their Morphology-Dependent Pseudocapacitive Performances, *Electrochim. Acta*, 2014, **133**, 382–390, DOI: 10.1016/j.electacta.2014.04.070.

24 N. Girija, S. S. Kuttan, B. N. Nair and U. N. Saraswathy Hareesh, Morphology control in nickel cobaltite synthesised *via* solution routes for electrochemical applications, *Results Eng.*, 2022, **15**, 100536, DOI: 10.1016/j.rineng.2022.100536.

25 A. K. Das, *et al.*, Facile synthesis of NiCo 2 O 4 Nanorods for Electrocatalytic Oxidation of, *J. Saudi Chem. Soc.*, 2020, (5), 434–444, DOI: 10.1016/j.jscs.2020.03.007.

26 M. Yu, *et al.*, Additive-free macroscopic-scale synthesis of coral-like nickel cobalt oxides with hierarchical pores and their electrocatalytic properties for methanol oxidation, *Electrochim. Acta*, 2014, **145**, 300–306, DOI: 10.1016/j.electacta.2014.07.131.

27 R. Ding, L. Qi, M. Jia and H. Wang, Simple hydrothermal synthesis of mesoporous spinel NiCo2O 4 nanoparticles and their catalytic behavior in CH3OH electro-oxidation and H2O2 electro-reduction, *Catal. Sci. Technol.*, 2013, **3**(12), 3207–3215, DOI: 10.1039/c3cy00590a.

28 J. Hong, S. J. Park and S. Kim, Synthesis and electrochemical characterization of nanostructured Ni-Co-MOF/graphene oxide composites as capacitor electrodes, *Electrochim. Acta*, 2019, **311**, 62–71, DOI: 10.1016/j.electacta.2019.04.121.

29 H. Q. Wang, *et al.*, Porous nano-MnO2: Large scale synthesis *via* a facile quick-redox procedure and application in a supercapacitor, *New J. Chem.*, 2011, **35**(2), 469–475, DOI: 10.1039/c0nj00712a.

30 M. Naseri, *et al.*, Structure and physical properties of NiO/Co3O4 nanoparticles, *Metals*, 2016, **6**(8), DOI: 10.3390/met6080181.

31 R. P. Raj, P. Ragupathy and S. Mohan, Remarkable capacitive behavior of a Co3O4-polyindole composite as electrode material for supercapacitor applications, *J. Mater. Chem. A*, 2015, **3**(48), 24338–24348, DOI: 10.1039/c5ta07046e.

32 L. Hu, J. Xu, S. Zhao, X. Li, L. Li and L. Ran, Red/Black Phosphorus Z-Scheme Heterogeneous Junction Modulated by Co-MOF for Enhanced Photocatalytic Hydrogen Evolution, *Catal. Lett.*, 2021, **151**(9), 2658–2672, DOI: 10.1007/s10562-020-03507-2.

33 M. G. Radhika, *et al.*, Electrochemical studies on Ni, Co & Ni/Co-MOFs for high-performance hybrid supercapacitors, *Mater. Res. Express*, 2020, **7**(5), DOI: 10.1088/2053-1591/ab8d5d.

34 D. Guragain, C. Zequine, T. Poudel, D. Neupane, R. K. Gupta and S. R. Mishra, Influence of Urea on the Synthesis of NiCo 2 O 4 Nanostructure: Morphological and Electrochemical Studies, *J. Nanosci. Nanotechnol.*, 2019, **20**(4), 2526–2537, DOI: 10.1166/jnn.2020.17366.

35 N. Narayanan and N. Bernaurdshaw, Reduced Graphene Oxide Supported $NiCo_2O_4$ Nano-Rods: An Efficient, Stable and Cost-Effective Electrocatalyst for Methanol Oxidation

Reaction, *ChemCatChem*, 2020, **12**(3), 771–780, DOI: **10.1002/cctc.201901496**.

36 E. Umeshbabu, G. Rajeshkhanna, P. Justin and G. R. Rao, Magnetic, optical and electrocatalytic properties of urchin and sheaf-like $NiCo_2O_4$ nanostructures, *Mater. Chem. Phys.*, 2015, **165**, 235–244, DOI: **10.1016/j.matchemphys.2015.09.023**.

37 E. Umeshbabu and G. Ranga Rao, $NiCo_2O_4$ hexagonal nanoplates anchored on reduced graphene oxide sheets with enhanced electrocatalytic activity and stability for methanol and water oxidation, *Electrochim. Acta*, 2016, **213**, 717–729, DOI: **10.1016/j.electacta.2016.07.161**.

38 P. Sennu, V. Aravindan and Y. S. Lee, High energy asymmetric supercapacitor with 1D@2D structured $NiCo_2O_4$@Co3O4 and jackfruit derived high surface area porous carbon, *J. Power Sources*, 2016, **306**, 248–257, DOI: **10.1016/j.jpowsour.2015.12.029**.

39 L. Gu, *et al.*, Microwave-assisted synthesis of nanosphere-like NiCo2O 4 consisting of porous nanosheets and its application in electro-catalytic oxidation of methanol, *J. Power Sources*, 2014, **261**, 317–323, DOI: **10.1016/j.jpowsour.2014.03.098**.

40 G. A. Ferrero, K. Preuss, A. B. Fuertes, M. Sevilla and M. M. Titirici, The influence of pore size distribution on the oxygen reduction reaction performance in nitrogen doped carbon microspheres, *J. Mater. Chem. A*, 2016, **4**(7), 2581–2589, DOI: **10.1039/c5ta10063a**.

41 M. Yu, *et al.*, Electrochimica Acta Mesoporous $NiCo_2O_4$ nanoneedles grown on 3D graphene-nickel foam for supercapacitor and methanol electro-oxidation, *Electrochim. Acta*, 2015, **151**, 99–108.

42 S. Liu, L. Hu, X. Xu, A. A. Al-ghamdi, and X. Fang, *Nickel Cobaltite Nanostructures for Photoelectric and Catalytic Applications*, 2015, 34, pp. 4267–4283, DOI: **10.1002/smll.201500315**.

43 W. M. A. El and A. Enaiet, *Oxidation in Basic Electrolytes †*, 2023, pp. 27934–27945, DOI: **10.1039/D3RA05105F**.

44 M. U. A. Prathap, B. Satpati and R. Srivastava, Electrochimica Acta Facile preparation of -Ni(OH)$_2$-$NiCo_2O_4$ hybrid nanostructure and its application in the electro-catalytic oxidation of methanol, *Electrochim. Acta*, 2014, **130**, 368–380, DOI: **10.1016/j.electacta.2014.03.043**.

45 W. Wang, Q. Chu, Y. Zhang, W. Zhu, X. Wang and X. Liu, Nickel foam supported mesoporous $NiCo_2O_4$ arrays with excellent methanol electro-oxidation performance, *New J. Chem.*, 2015, **39**(8), 6491–6497, DOI: **10.1039/c5nj00766f**.

46 M. Silambarasan, P. S. Ramesh and D. Geetha, Facile one-step synthesis, structural, optical and electrochemical properties of $NiCo_2O_4$ nanostructures, *J. Mater. Sci. Mater. Electron.*, 2017, **28**(1), 323–336, DOI: **10.1007/s10854-016-5527-9**.

47 A. K. Das, R. K. Layek, N. H. Kim, D. Jung and J. H. Lee, Reduced graphene oxide (RGO)-supported $NiCo_2O_4$ nanoparticles: An electrocatalyst for methanol oxidation, *Nanoscale*, 2014, **6**(18), 10657–10665, DOI: **10.1039/c4nr02370f**.

48 F. Paquin, J. Rivnay, A. Salleo, N. Stingelin and C. Silva, Multi-phase semicrystalline microstructures drive exciton dissociation in neat plastic semiconductors, *J. Mater. Chem. C*, 2015, **3**, 10715–10722, DOI: **10.1039/b000000x**.

49 A. K. Das, R. K. Layek, N. H. Kim, D. Jung and J. H. Lee, Reduced graphene oxide (RGO)-supported $NiCo_2O_4$ nanoparticles: An electrocatalyst for methanol oxidation, *Nanoscale*, 2014, **6**(18), 10657–10665, DOI: **10.1039/c4nr02370f**.

50 D. Chakraborty, I. Chorkendorff and T. Johannessen, Electrochemical impedance spectroscopy study of methanol oxidation on nanoparticulate PtRu direct methanol fuel cell anodes: Kinetics and performance evaluation, *J. Power Sources*, 2006, **162**(2), 1010–1022, DOI: **10.1016/j.jpowsour.2006.08.010**.

51 Y. Song, X. Zhang, S. Yang, X. Wei and Z. Sun, Electrocatalytic performance for methanol oxidation on nanoporous Pd/NiO composites prepared by one-step dealloying, *Fuel*, 2016, **181**, 269–276, DOI: **10.1016/j.fuel.2016.04.086**.

52 S. S. Mahapatra, A. Dutta and J. Datta, Temperature dependence on methanol oxidation and product formation on Pt and Pd modified Pt electrodes in alkaline medium, *Int. J. Hydrogen Energy*, 2011, **36**(22), 14873–14883, DOI: **10.1016/j.ijhydene.2010.11.085**.

53 E. Umeshbabu and G. Ranga Rao, $NiCo_2O_4$ hexagonal nanoplates anchored on reduced graphene oxide sheets with enhanced electrocatalytic activity and stability for methanol and water oxidation, *Electrochim. Acta*, 2016, **213**, 717–729, DOI: **10.1016/j.electacta.2016.07.161**.

54 K. Chaitra, N. Nagaraju and K. Nagaraju, Nanocomposite of hexagonal β-Ni(OH)2/multiwalled carbon nanotubes as high performance electrode for hybrid supercapacitors, *Mater. Chem. Phys.*, 2015, **164**, 98–107, DOI: **10.1016/j.matchemphys.2015.08.030**.

55 Z. Li, *et al.* Synergistic coupling of FeNi3 alloy with graphene carbon dots for advanced oxygen evolution reaction electrocatalysis, *J. Colloid Interface Sci.*, 2022, **615**, 273–281.